

Impact of conversion-driven processes on singlet-doublet Majorana dark matter relic

Partha Kumar Paul ^{1,*} Sujit Kumar Sahoo ^{1,†} and Narendra Sahu ^{1,‡}

¹*Department of Physics, Indian Institute of Technology Hyderabad, Kandi, Telangana-502285, India.*

(Dated: November 19, 2025)

The singlet-doublet dark matter model offers a rich framework for exploring the nature of dark matter (DM) through its unique fermion structure. In this model, the important parameters are singlet-doublet mass splitting ΔM , singlet-doublet mixing angle $\sin\theta$, and DM mass M_{DM} . If the DM is assumed to be of Dirac nature, then the annihilation, co-annihilation, and conversion driven processes combinedly allows a range of parameter space: $1 \text{ GeV} \lesssim M_{\text{DM}} \lesssim 750 \text{ GeV}$ and $10^{-6} \lesssim \sin\theta \lesssim 0.04$ for all $\Delta M > 1 \text{ GeV}$. While the nature of DM either Dirac or Majorana is not known, in this work we assume the nature of singlet-doublet DM to be of Majorana type and find that the relic density and direct detection can be satisfied in a larger parameter space. In particular, the allowed ranges of DM mass and $\sin\theta$ are: $1 \text{ GeV} \lesssim M_{\text{DM}} \lesssim 1750 \text{ GeV}$ and $2 \times 10^{-7} \lesssim \sin\theta \lesssim 0.16$ for all $\Delta M > 1 \text{ GeV}$.

I. INTRODUCTION

Dark matter (DM) constitutes approximately 26.8% of the Universe's total energy budget ($\Omega_{\text{DM}} h^2 \simeq 0.12$) [1], evidencing its presence through galaxy rotation curves, gravitational lensing, the formation of large-scale structures, etc [2, 3]. Given the absence of a DM candidate within the standard model, the Weakly Interacting Massive Particle (WIMP) emerges as a compelling contender, capable of accounting for the DM relic density through freeze-out processes in the early Universe. A simple extension of the SM for the explanation of DM could be a singlet fermion, which is odd under \mathcal{Z}_2 symmetry. However, the parameter space faces stringent constraints from both relic density requirements and direct detection experiments [4, 5]. Another alternative would be to consider a \mathcal{Z}_2 odd doublet fermion which also fails due to excessive annihilation and detection constraints. These issues can be resolved if one considers the combination of singlet and doublet fermion together. The neutral component of the doublet mixes with the singlet fermion to give the so-called fermionic singlet-doublet DM (SDDM) [4–34]. The attractive part of this model is that it is very minimal model in the BSM scenario having only three parameters: DM mass M_{DM} , singlet-doublet (SD) mixing $\sin\theta$, and SD mass splitting ΔM . This model not only predict the DM relic but also facilitate probes at different terrestrial experiments. The DM relic is not only decided by annihilation and co-annihilation processes but also by conversion-driven [35, 36] processes (which includes co-scattering, decay and inverse-decay). It was found that if the SD mixing is large (typically $\sin\theta \gtrsim 0.05$) annihilation and co-annihilation processes decide the relic [4]. On the other hand, in the small mixing angle limits, the conversion-driven processes plays an important role in deciding the relic of the DM. It was shown that for

$0.05 \gtrsim \sin\theta \gtrsim 10^{-6}$ the singlet can be brought to equilibrium. However for small $\sin\theta$ the singlet component decouples early with a larger abundance. Nevertheless, through the conversion-driven processes the DM particles scatter into a higher mass state within the dark sector such as the doublet, thereby reducing the singlet abundance. As a result final relic of the DM can be brought to the correct ball park even if the $\sin\theta$ is small. For $\sin\theta < 10^{-7}$, the singlet never attains equilibrium. In this case, the relic can be achieved by the non-thermal mechanisms such as SuperWIMP and freeze-in. Assuming the SDDM to be Dirac type, the full parameter space of DM relic including annihilation, co-annihilation, co-scattering, decay, and inverse decay was estimated in [34]. In fact the allowed parameter space for a Dirac SDDM was found to be $1 \text{ GeV} \lesssim M_{\text{DM}} \lesssim 750 \text{ GeV}$ and $10^{-6} \lesssim \sin\theta \lesssim 0.04$ for $\Delta M > 1 \text{ GeV}$. On the other hand, in the Majorana fermionic DM scenario, where the DM particle is its own antiparticle, its dynamics or the relic-determining processes differ from those of its Dirac counterpart. Consequently, this distinction leads to a modified parameter space for Majorana DM candidates.

In this paper, we assume the SDDM to be of Majorana type and studied the allowed parameter space for the correct relic density including annihilation, co-annihilation and conversion-driven processes. We show that in case of Majorana SDDM the correct relic density allows the ranges of DM mass and $\sin\theta$ are: $1 \text{ GeV} \lesssim M_{\text{DM}} \lesssim 1750 \text{ GeV}$ and $2 \times 10^{-7} \lesssim \sin\theta \lesssim 0.16$ for $\Delta M > 1 \text{ GeV}$. We also note that inclusion of the conversion-driven processes shifts the relic parameter space to the sensitivity ranges of LHC [40] and MATHUSLA [41].

The paper is organized as follows. In section II, we describe the singlet-doublet Majorana DM model in detail. The DM phenomenology and detection prospects are discussed in section III. We finally conclude in section IV.

II. THE MODEL

The standard model (SM) is extended with a singlet fermion, χ , and a doublet fermion, $\Psi = (\psi^0 \ \psi^-)^T =$

* ph22resch11012@iith.ac.in

† ph21resch11008@iith.ac.in

‡ nsahu@phy.iith.ac.in

$(\psi_L^0 + \psi_R^0 \quad \psi^-)^T$ which are odd under a discrete symmetry \mathcal{Z}_2 . The DM Lagrangian can be written as

$$\begin{aligned} \mathcal{L}_{\text{DM}} = & \bar{\Psi} i \gamma^\mu \mathcal{D}_\mu \Psi - M_\Psi \bar{\Psi} \Psi + \bar{\chi} i \gamma^\mu \partial_\mu \chi - \frac{1}{2} M_\chi \bar{\chi} \chi \\ & - \frac{y_\chi}{\sqrt{2}} \bar{\Psi} \tilde{H} (\chi + \chi^c) + h.c. \end{aligned} \quad (1)$$

The neutral fermion mass matrix can be written in the basis: $((\psi_R^0)^c, \psi_L^0, (\chi)^c)^T$ as

$$\begin{pmatrix} 0 & M_\Psi & \frac{m_D}{\sqrt{2}} \\ M_\Psi & 0 & \frac{m_D}{\sqrt{2}} \\ \frac{m_D}{\sqrt{2}} & \frac{m_D}{\sqrt{2}} & M_\chi \end{pmatrix}, \quad (2)$$

where $m_D = y_\chi v_h / \sqrt{2}$, and v_h is the vacuum expectation value (vev) of the SM Higgs boson, H . The mass matrix can be diagonalized with a unitary matrix of the form $U(\theta) = U_{13}(\theta_{13} = \theta).U_{23}(\theta_{23} = 0).U_{12}(\theta_{12} = \frac{\pi}{4})$. The three neutral states mix and give three Majorana states as $\chi_i = \frac{\chi_{iL} + \chi_{iL}^c}{\sqrt{2}}$, where

$$\begin{aligned} \chi_{1L} &= \frac{\cos \theta}{\sqrt{2}} (\psi_L^0 + (\psi_R^0)^c) + \sin \theta N_1^c, \\ \chi_{2L} &= \frac{i}{\sqrt{2}} (\psi_L^0 - (\psi_R^0)^c), \\ \chi_{3L} &= -\frac{\sin \theta}{\sqrt{2}} (\psi_L^0 + (\psi_R^0)^c) + \cos \theta N_1^c. \end{aligned} \quad (3)$$

The corresponding mass eigenvalues are

$$\begin{aligned} M_{\chi_1} &= M_\Psi \cos^2 \theta + M_\chi \sin^2 \theta + m_D \sin 2\theta, \\ M_{\chi_2} &= M_\Psi, \\ M_{\chi_3} &= M_\Psi \sin^2 \theta + M_\chi \cos^2 \theta - m_D \sin 2\theta, \end{aligned} \quad (4)$$

where the mixing angle is given as

$$\tan 2\theta = \frac{2m_D}{M_\Psi - M_{\chi_3}}. \quad (5)$$

Here we consider M_{χ_3} to be the lightest among the dark sector particles and identify the χ_3 as the DM candidate with $M_{\chi_3} = M_{\text{DM}}$. The Yukawa coupling can be expressed as,

$$y_\chi = \frac{\Delta M \sin 2\theta}{\sqrt{2} v_h}, \quad (6)$$

where the SD mass splitting, $\Delta M = M_{\chi_1} - M_{\chi_3}$.

III. DARK MATTER PHENOMENOLOGY AND DETECTION PROSPECTS

We investigate the DM phenomenology of the SDDM model, considering a singlet Majorana fermion as the DM candidate within a thermal freeze-out framework. A comprehensive numerical scan is performed over the model parameter space, incorporating conversion-driven processes alongside conventional annihilation and co-annihilation mechanisms. The analysis explores the viable mass range for the DM candidate between 10 GeV and 2000 GeV. In earlier studies of the SDDM framework [5], it was commonly assumed that all dark sector particles decouple simultaneously. However, this assumption does not necessarily hold for small mixing angles. In particular, for values of $\sin \theta \lesssim 0.05$, the DM particles fail to maintain chemical equilibrium with the thermal bath. Consequently, the singlet typically decouples earlier, while the doublet remains in equilibrium for a longer period owing to its gauge interactions. In accordance with that, we consider three distinct sectors in order to trace the evolution of DM independently from other particles in the thermal bath. The DM component is assigned to sector 1, while the remaining dark sector particles belong to sector 2 and the SM particles constitute sector 0. In this setup, particles in sectors 1 and 2 can interact mutually and with sector 0 (i.e., SM particles). Consequently, the cosmological evolution of sectors 1 and 2 must be tracked simultaneously. The Boltzmann equations governing the evolution of the comoving number densities of sector 1 and sector 2, defined as $Y_1 (= n_1/s)$ and $Y_2 (= n_2/s)$, respectively, where $n_i (i \in \{1, 2\})$ denotes the number density of i th sector and $s = 2\pi^2 g_{*s} T^3 / 45$ represents the entropy density, are given by [34, 38],

$$\begin{aligned} \frac{dY_1}{dT} = & \frac{1}{3\mathcal{H}} \frac{ds}{dT} \left[\langle \sigma_{1100} v \rangle (Y_1^2 - Y_1^{\text{eq}2}) + \langle \sigma_{1122} v \rangle \left(Y_1^2 - Y_2^2 \frac{Y_1^{\text{eq}2}}{Y_2^{\text{eq}2}} \right) + \langle \sigma_{1200} v \rangle (Y_1 Y_2 - Y_1^{\text{eq}} Y_2^{\text{eq}}) \right. \\ & \left. + \langle \sigma_{1222} v \rangle \left(Y_1 Y_2 - Y_2^2 \frac{Y_1^{\text{eq}}}{Y_2^{\text{eq}}} \right) - \langle \sigma_{1211} v \rangle \left(Y_1 Y_2 - Y_1^2 \frac{Y_2^{\text{eq}}}{Y_1^{\text{eq}}} \right) - \frac{\Gamma_{2 \rightarrow 1}}{s} \left(Y_2 - Y_1 \frac{Y_2^{\text{eq}}}{Y_1^{\text{eq}}} \right) \right], \end{aligned} \quad (7)$$

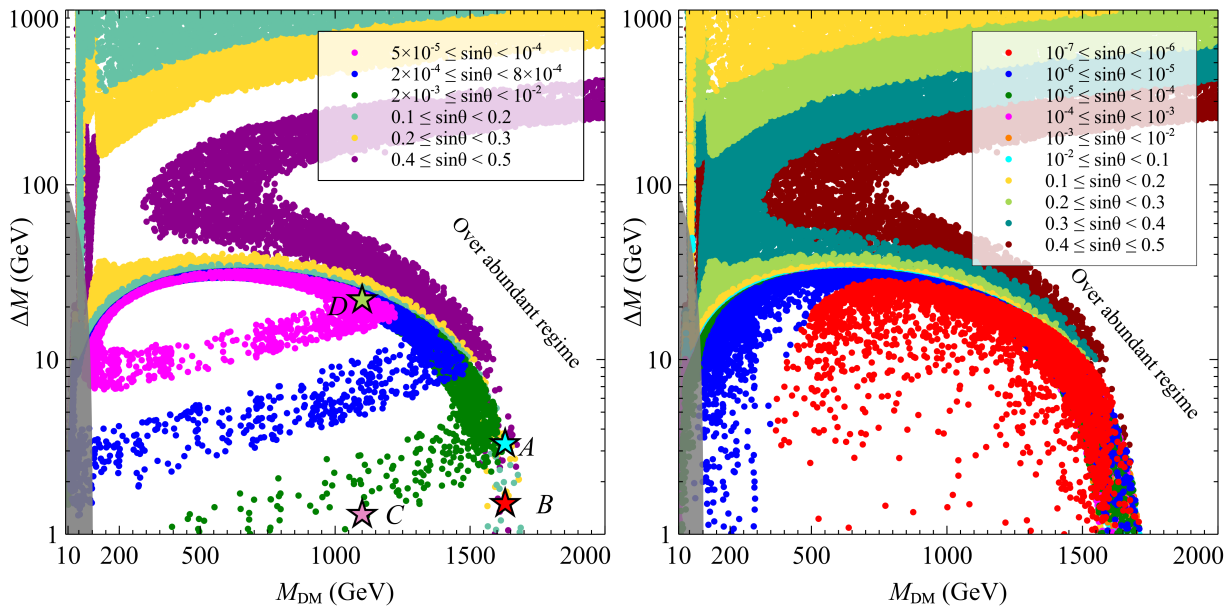


FIG. 1. [Left:] correct dark matter relic points are shown in the plane of ΔM vs M_{DM} for different ranges of $\sin \theta$ as mentioned in the inset of the figure without considering co-scattering contributions while solving Eqs. (7) and (8). [Right:] correct dark matter relic points are shown in the plane of ΔM vs M_{DM} for different ranges of $\sin \theta$ as mentioned in the inset of the figure considering all the relevant contributions including annihilation, co-annihilation, co-scattering and decay, inverse-decay while solving Eqs. (7) and (8). The gray region is excluded from the LEP bound [37].

TABLE I. Relic density for benchmark points are given: (a) without considering co-scattering, and (b) without considering co-scattering and decay.

Point	M_{DM} (GeV)	ΔM (GeV)	$\sin \theta$	$\Omega_{2s} h^2$ (no co-scattering)	$\Omega_{2s} h^2$ (no co-scattering) without decay
A	1630	3.3	9.5×10^{-3}	0.12	0.896
B	1630	1.5	9.5×10^{-3}	0.21	0.796
C	1100	1.3	9.5×10^{-3}	0.12	1.21
D	1100	22	9.5×10^{-3}	0.12	5.1

$$\begin{aligned}
 \frac{dY_2}{dT} = & \frac{1}{3\mathcal{H}} \frac{ds}{dT} \left[\langle \sigma_{2200} v \rangle (Y_2^2 - Y_2^{\text{eq}2}) - \langle \sigma_{1122} v \rangle \left(Y_1^2 - Y_2^2 \frac{Y_1^{\text{eq}2}}{Y_2^{\text{eq}2}} \right) + \langle \sigma_{1200} v \rangle (Y_1 Y_2 - Y_1^{\text{eq}} Y_2^{\text{eq}}) \right. \\
 & \left. - \langle \sigma_{1222} v \rangle \left(Y_1 Y_2 - Y_2^2 \frac{Y_1^{\text{eq}}}{Y_2^{\text{eq}}} \right) + \langle \sigma_{1211} v \rangle \left(Y_1 Y_2 - Y_1^2 \frac{Y_2^{\text{eq}}}{Y_1^{\text{eq}}} \right) + \frac{\Gamma_{2 \rightarrow 1}}{s} \left(Y_2 - Y_1 \frac{Y_2^{\text{eq}}}{Y_1^{\text{eq}}} \right) \right], \quad (8)
 \end{aligned}$$

where $Y_i^{\text{eq}} (= n_i^{\text{eq}}/s)$ are the equilibrium abundances, $\mathcal{H} = 1.66 \sqrt{g_*} \frac{T^2}{M_{\text{Pl}}}$ is the Hubble parameter with $M_{\text{Pl}} = 1.22 \times 10^{19}$ GeV being the Planck mass, and $\langle \sigma_{\alpha\beta\gamma\delta} v \rangle$ are the thermally averaged cross-sections for the processes $\alpha\beta \leftrightarrow \gamma\delta$. The term $\Gamma_{2 \rightarrow 1}$ in Eq. (8) includes the interaction rate of both decay, $\Gamma_{2 \rightarrow 1,0}$ and co-scattering, $n_{\text{SM}}^{\text{eq}} \langle \sigma_{2010} v \rangle$ with $n_{\text{SM}}^{\text{eq}} = 0.238 \times s$.

In the *left* panel of Fig. 1, we present the parameter space yielding the observed relic abundance in the ΔM – M_{DM} plane, obtained by numerically solving Eqs. (7) and (8) without incorporating the co-scattering contributions in the $\Gamma_{2 \rightarrow 1}$ term. The different colors correspond to distinct ranges of the SD mixing angle

$\sin \theta$, as indicated in the figure inset. For each color band, the region to its right corresponds to an overabundant relic density, whereas the region to its left leads to an underabundant relic density. At larger mass splittings ($\Delta M \gtrsim 100$ GeV), DM interacts with SM bath via annihilation processes providing a correct freeze-out relic, while for smaller ΔM ($\Delta M \lesssim 100$ GeV), the co-annihilation processes become dominant in comparison to the annihilation processes. Nevertheless the decay and inverse-decay processes also play significant role to maintain equilibrium among the sector 1 and sector 2 particles [34]. As the DM mass increases, the cross-section decreases. To enhance the cross-section, in the annihilation dominating region, ΔM has to be increased to get

the relic of DM in the correct ballpark. For the same reason, in the co-annihilation dominating region, ΔM has to be reduced to obtain correct relic density. This is why, for $\sin\theta \gtrsim 10^{-1}$, we see an upward trend in ΔM in the region $\Delta M \gtrsim 100$ GeV, while a downward trend in ΔM for $\Delta M \lesssim 100$ GeV with increase in DM mass. In the small $\sin\theta$ ($\lesssim 10^{-2}$) region, the dominating processes that decide the relic density are co-annihilation, decay and inverse-decay. In this region, due to the interplay between co-annihilation and decay and inverse-decay processes¹, there exists a maximum allowed M_{DM} for each $\sin\theta$ beyond which the relic remains overabundant. To understand this behavior, we have provided four benchmark points, namely *A, B, C* and *D* in table I. Say for BP-*A* ($\sin\theta = 9.5 \times 10^{-3}$), $\Delta M = 3.3$ GeV gives correct relic abundance as shown in the left panel of Fig. 1. If we switch off the term $\Gamma_{2 \rightarrow 1}$ while solving Eqs. (7) and (8) (i.e. without including the effect of co-scattering, decay and inverse-decay processes), the same set of parameters result in a slightly increased relic density as shown in the table I. This is because the rate of co-annihilation processes get diminished for this small $\sin\theta$ leading to an overabundant relic which can be brought to the correct ballpark in presence of decay and inverse-decay processes. Now in BP-*B*, we keep the M_{DM} and $\sin\theta$ same as BP-*A*, but with a smaller $\Delta M = 1.5$ GeV. This small ΔM reduces the effect of decay and inverse-decay and with this small $\sin\theta$, the co-annihilation effects are not sufficient enough, leading to an overabundant BP-*B*. However, we note that by increasing the $\sin\theta$ the relic density of BP-*B* can be brought to correct ballpark. In BP-*C* ($\Delta M = 1.3$ GeV and $\sin\theta$ same as point *A*), we consider a smaller $M_{\text{DM}} = 1100$ GeV, which results in an increased interaction rate of co-annihilation processes leading to a correct relic density. Similarly, we have considered another BP-*D*, with same M_{DM} and $\sin\theta$ as that of *C*, but with a larger ΔM . We note that *D* also gives correct relic density due to an enhanced decay and inverse-decay effects without which the relic would have been enhanced significantly as shown in the table I.

So far we have switched off the co-scattering effects while solving Eqs. (7) and (8). Now we solve the Eqs. (7) and (8) without switching off the co-scattering processes and showcase the correct relic points in the plane of M_{DM} and ΔM in the *right* panel of Fig. 1. The various colored points represent the range of $\sin\theta$ as given in the inset of the figure. For $\sin\theta \gtrsim 0.05$, the annihilation, co-annihilation, decay and inverse-decay processes are sufficient enough to keep the DM in equilibrium with SM bath until the sector 2 particles decouple from SM. This is the reason, co-scattering processes do not play any role in large $\sin\theta$ region. As the $\sin\theta$ decreases, DM decouples chemically from thermal bath early, while the sector

2 particles still interact with SM bath because of their gauge interactions. Treating the evolution of the singlet and doublet separately, we find that for smaller $\sin\theta$ and ΔM , the singlet decouples early with a larger abundance. However, the number density of the singlet, which is the sector 1 particle, gets converted to the sector 2 particles through the conversion-driven processes. The sector 2 particles being in thermal equilibrium get converted to SM particles via the “2200” processes. As a result, the DM number density keeps depleting until to reach the correct value.

To illustrate the effects of co-scattering and decay, we choose two sets of benchmark points as mentioned in the table II. We show the cosmological evolution of the abundances of *BP1* in the *left* panel of Fig. 2. The blue (red) solid and dashed lines represent the abundance of the singlet (doublet) and its equilibrium values, respectively. We see that the large mixing angle leads to a simultaneous decoupling of the singlet and doublet components around $z \sim 24.5$. In this case, the relic is determined by the co-annihilation processes. The annihilation processes are subdominant because of the small mass splitting. We now move to *BP2*. Here, we see that the singlet decouples very early, around $z \sim 19$, whereas the doublet stays in equilibrium due to its gauge interactions up to $z \sim 25.2$. Although the singlet decouples with a larger abundance, because of the co-scattering and decay processes, its relic gets reduced to the observed value with the help of 2200 processes.

In the right panel of Fig. 1, we show the correct DM relic density points by solving Eqs. (7) and (8) taking in to the effects of all processes namely annihilation, co-annihilation, co-scattering, decay and inverse-decay. The parameter space that previously yielded the correct relic density when co-scattering was excluded get under abundant in presence of the co-scattering processes. On the other hand, the over-abundant points with $\sin\theta < 10^{-5}$, which did not provide the correct relic density in the absence of co-scattering processes, now yield the correct relic density once these processes are included.

To demonstrate the effect of co-scattering quantitatively, we define a new parameter,

$$\rho_2 = \frac{\Omega_{2s} h^2}{\Omega_{2s} h^2 (\text{no coscattering})}, \quad (9)$$

where $\Omega_{2s} h^2$ is obtained by solving Eqs. (7) and (8) which takes in to account the effects of co-scattering in addition to all other number-changing processes, such as decay, inverse decay, annihilation, and co-annihilation. In contrast, $\Omega_{2s} h^2$ (no co-scattering) refers to the relic density computed by solving Eqs. (7) and (8) while switching off the co-scattering processes in $\Gamma_{2 \rightarrow 1}$. According to the definition of ρ_2 provided in Eq. (9), a value of $\rho_2 = 1$ signifies that the relic density is independent of co-scattering effects. Consequently, any deviation from unity indicates the influence of co-scattering on the final relic density. The magnitude of this deviation serves as a measure of the impact of co-scattering; specifically,

¹ Note that the interaction rate of co-annihilation processes enhances with reduction in ΔM , while the decay width decreases with decrease in ΔM

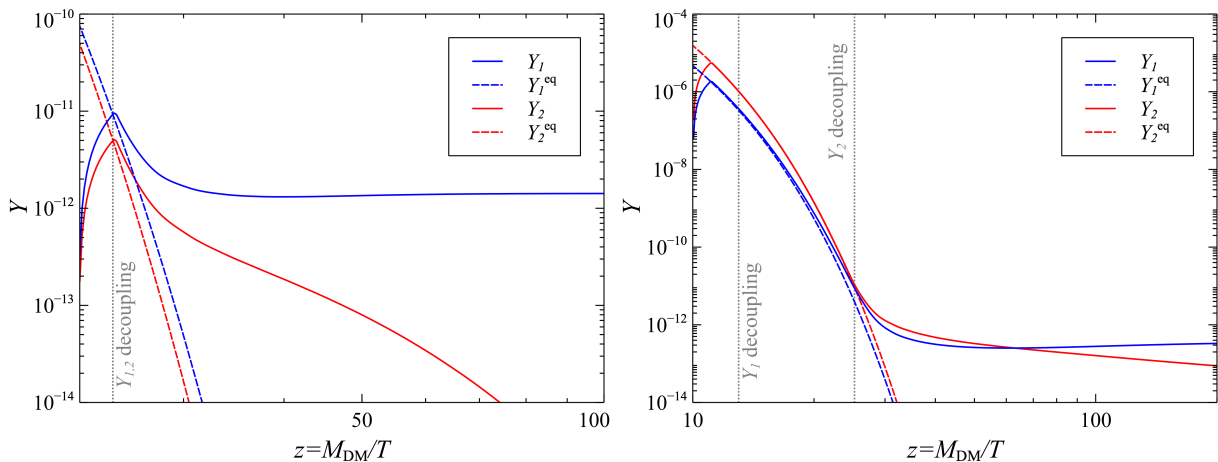


FIG. 2. Cosmological evolution of abundances of sector 1 and sector 2 particles for two sets of parameters illustrating co-annihilation (*left*) and co-scattering and decay effects (*right*). The parameters are mentioned in table II .

TABLE II. Benchmark points for the evolution of dark sector abundances. These two points are also shown with a yellow star and a yellow diamond in Fig. 3.

Benchmark Points	M_{DM} (GeV)	ΔM (GeV)	$\sin \theta$
BP1	285.721	24.5826	0.039039
BP2	972.047	21.6068	6.97978×10^{-7}

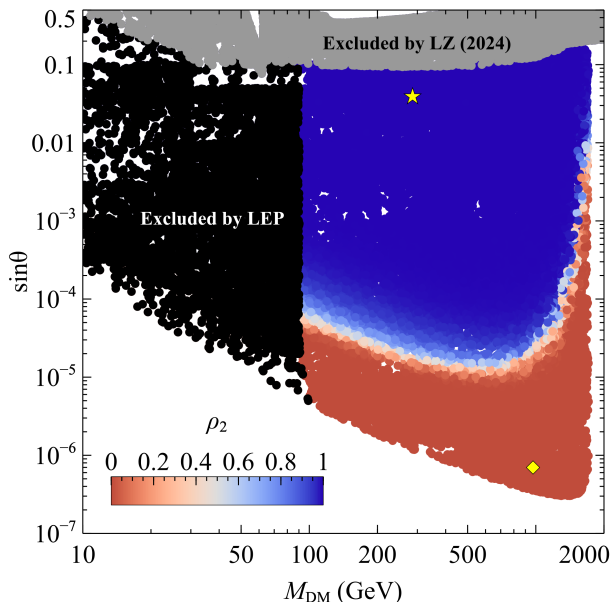


FIG. 3. Correct dark matter relic points are shown in the plane of $\sin \theta$ vs M_{DM} . The color code represents the parameter ρ_2 . The gray shaded region is excluded by direct detection experiment LZ [39]. LEP [37] constraint on the doublet fermion excludes the black shaded region.

a larger deviation corresponds to a more significant effect from co-scattering. Moreover, as mentioned, $\Omega_{2s} h^2$ encompasses all relevant processes, including annihilation, co-annihilation, co-scattering, and decay, whereas

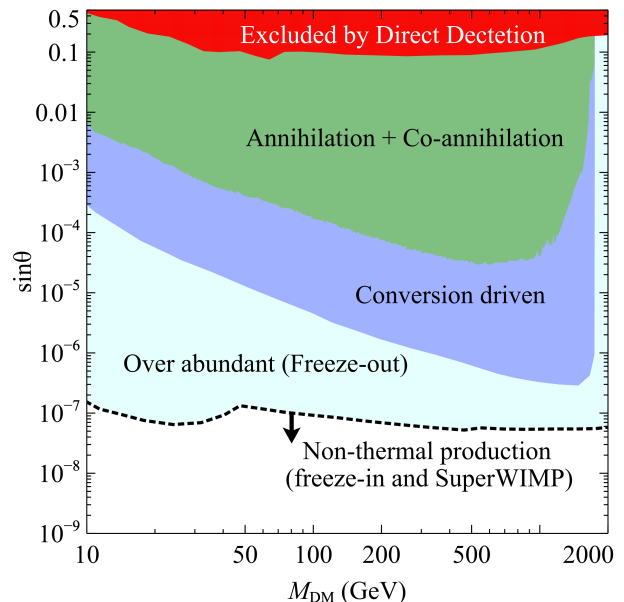


FIG. 4. Phase diagram illustrating the SDDM parameter space. The black dashed line separates the thermal regime (above) from the non-thermal regime (below).

$\Omega_{2s} h^2$ (no co-scattering) is limited to the processes of annihilation, co-annihilation, and decay. This distinction implies that the effective cross-section associated with $\Omega_{2s} h^2$ is always greater than or equal to that of $\Omega_{2s} h^2$ (no co-scattering). Therefore, we can conclude that: $\Omega_{2s} h^2 \leq \Omega_{2s} h^2$ (no co-scattering), which leads to

$\rho_2 \leq 1$.

In Fig. 3, we present the correct relic satisfying points in the plane of $\sin\theta - M_{\text{DM}}$. The color map depicts the ρ_2 values. The blue colored points correspond to $\rho_2 \simeq 1$. This represents the parameter space where co-scattering effects are negligible and the relic is decided solely by annihilation and/or co-annihilation processes. As $\sin\theta$ decreases, ρ_2 deviates from unity, pointing towards the increasing significance of co-scattering processes across a wider parameter space shown with the light bluish and brown colored regions. For the illustration purpose we have shown the *BP1* and *BP2* in Fig. 3. It is straight forward to note that even $\sin\theta$ is quite different for *BP1* and *BP2*, they can give rise to correct relic density due to the significance of different processes involved in relic computation. Below the colored region, even though the DM can be produced thermally, the conversion-driven processes, including decay, inverse decay, and co-scattering, are not efficient in producing the correct relic of DM leading to an over abundant relic. If the $\sin\theta$ is reduced further, the DM can never be thermalized. The relic, in this case, is determined by non-thermal processes such as freeze-in and SuperWIMP mechanisms [34].

Displaced vertex signatures: We note that the doublet fermion (ψ^\pm) can be produced because of their gauge interaction which further can decay to DM and charge leptons via the singlet doublet mixing through off-shell gauge boson exchange. This can give rise displaced vertex signatures in the LHC [40] and, in future, MATHUSLA [41]. As already discussed, conversion-driven processes allows smaller $\sin\theta$ ($\lesssim \mathcal{O}(10^{-3})$) which results in smaller decay widths of ψ^\pm . Thereby increasing the decay length which can fall in the reaches of LHC and MATHUSLA [34].

IV. CONCLUSION AND FUTURE OUTLOOK

In this work, we analyzed the parameter space of the singlet-doublet Majorana DM considering thermal freeze-

out scenario. We found that the maximum allowed $\sin\theta$ from direct detection is ~ 0.4 . The combined upper limit on the mixing angle from LZ and LEP lead to $\sin\theta \lesssim 0.16$. We summarize our analysis in Fig. 4, in the plane of M_{DM} and $\sin\theta$. In the green shaded region annihilation and co-annihilation processes contribute in deciding the relic of DM depending on the values of ΔM . In the blue shaded region conversion-driven processes decides the relic. In the cyan shaded region even though the DM can be in thermal equilibrium but due to such small $\sin\theta$ it decouples early with larger abundance. Conversion-driven processes are inefficient in this region. The black dashed line serves as the boundary, above which, DM can be brought to thermal equilibrium with SM thermal bath. In the region below the black dashed line, the DM never reaches thermal equilibrium because of the small SD mixing angle. We find the allowed ranges of DM mass and $\sin\theta$ for thermal relic of DM to be: $1 \text{ GeV} \lesssim M_{\text{DM}} \lesssim 1750 \text{ GeV}$ and $2 \times 10^{-7} \lesssim \sin\theta \lesssim 0.16$ for all $\Delta M > 1 \text{ GeV}$. We also note that incorporating conversion-driven processes substantially enlarges the region of parameter space accessible to both the LHC and MATHUSLA experiments.

ACKNOWLEDGEMENTS

P.K.P. would like to acknowledge the Ministry of Education, Government of India, for providing financial support for his research via the Prime Minister's Research Fellowship (PMRF) scheme.

-
- [1] N. Aghanim *et al.* (Planck), Planck 2018 results. VI. Cosmological parameters, *Astron. Astrophys.* **641**, A6 (2020), [Erratum: *Astron.Astrophys.* 652, C4 (2021)], [arXiv:1807.06209](https://arxiv.org/abs/1807.06209) [[astro-ph.CO](https://arxiv.org/abs/1807.06209)].
 - [2] F. Zwicky, Die Rotverschiebung von extragalaktischen Nebeln, *Helv. Phys. Acta* **6**, 110 (1933).
 - [3] V. C. Rubin and W. K. Ford, Jr., Rotation of the Andromeda Nebula from a Spectroscopic Survey of Emission Regions, *Astrophys. J.* **159**, 379 (1970).
 - [4] S. Bhattacharya, P. Ghosh, N. Sahoo, and N. Sahu, Mini Review on Vector-Like Leptonic Dark Matter, Neutrino Mass, and Collider Signatures, *Front. in Phys.* **7**, 80 (2019), [arXiv:1812.06505](https://arxiv.org/abs/1812.06505) [[hep-ph](https://arxiv.org/abs/1812.06505)].
 - [5] M. Dutta, S. Bhattacharya, P. Ghosh, and N. Sahu, Singlet-Doublet Majorana Dark Matter and Neutrino Mass in a minimal Type-I Seesaw Scenario, *JCAP* **03**, 008, [arXiv:2009.00885](https://arxiv.org/abs/2009.00885) [[hep-ph](https://arxiv.org/abs/2009.00885)].
 - [6] G. Cynolter, J. Kovács, and E. Lendvai, Doublet-singlet model and unitarity, *Mod. Phys. Lett.* **A31**, 1650013 (2016), [arXiv:1509.05323](https://arxiv.org/abs/1509.05323) [[hep-ph](https://arxiv.org/abs/1509.05323)].
 - [7] S. Bhattacharya, N. Sahoo, and N. Sahu, Minimal vectorlike leptonic dark matter and signatures at the LHC, *Phys. Rev. D* **93**, 115040 (2016), [arXiv:1510.02760](https://arxiv.org/abs/1510.02760) [[hep-ph](https://arxiv.org/abs/1510.02760)].
 - [8] S. Bhattacharya, N. Sahoo, and N. Sahu, Singlet-Doublet Fermionic Dark Matter, Neutrino Mass and Collider Signatures, *Phys. Rev. D* **96**, 035010 (2017), [arXiv:1704.03417](https://arxiv.org/abs/1704.03417) [[hep-ph](https://arxiv.org/abs/1704.03417)].
 - [9] S. Bhattacharya, P. Ghosh, and N. Sahu, Multipartite Dark Matter with Scalars, Fermions and signatures at LHC, *JHEP* **02**, 059, [arXiv:1809.07474](https://arxiv.org/abs/1809.07474) [[hep-ph](https://arxiv.org/abs/1809.07474)].

- [10] S. Bhattacharya, B. Karmakar, N. Sahu, and A. Sil, Flavor origin of dark matter and its relation with leptonic nonzero θ_{13} and Dirac CP phase δ , *JHEP* **05**, 068, [arXiv:1611.07419 \[hep-ph\]](#).
- [11] D. Borah, M. Dutta, S. Mahapatra, and N. Sahu, Lepton anomalous magnetic moment with singlet-doublet fermion dark matter in a scotogenic U(1) $L\mu$ -L τ model, *Phys. Rev. D* **105**, 015029 (2022), [arXiv:2109.02699 \[hep-ph\]](#).
- [12] D. Borah, M. Dutta, S. Mahapatra, and N. Sahu, Singlet-doublet self-interacting dark matter and radiative neutrino mass, *Phys. Rev. D* **105**, 075019 (2022), [arXiv:2112.06847 \[hep-ph\]](#).
- [13] D. Borah, S. Mahapatra, and N. Sahu, Singlet-doublet fermion origin of dark matter, neutrino mass and W-mass anomaly, *Phys. Lett. B* **831**, 137196 (2022), [arXiv:2204.09671 \[hep-ph\]](#).
- [14] D. Borah, S. Mahapatra, D. Nanda, S. K. Sahoo, and N. Sahu, Singlet-doublet fermion Dark Matter with Dirac neutrino mass, $(g - 2)_\mu$ and ΔN_{eff} , *JHEP* **05**, 096, [arXiv:2310.03721 \[hep-ph\]](#).
- [15] P. K. Paul, N. Sahu, and P. Shukla, Thermal leptogenesis, dark matter, and gravitational waves from an extended canonical seesaw scenario, *Phys. Rev. D* **112**, 015032 (2025), [arXiv:2409.08828 \[hep-ph\]](#).
- [16] R. Mahbubani and L. Senatore, The Minimal model for dark matter and unification, *Phys. Rev. D* **73**, 043510 (2006), [arXiv:hep-ph/0510064](#).
- [17] F. D'Eramo, Dark matter and Higgs boson physics, *Phys. Rev. D* **76**, 083522 (2007), [arXiv:0705.4493 \[hep-ph\]](#).
- [18] T. Cohen, J. Kearney, A. Pierce, and D. Tucker-Smith, Singlet-Doublet Dark Matter, *Phys. Rev. D* **85**, 075003 (2012), [arXiv:1109.2604 \[hep-ph\]](#).
- [19] A. Freitas, S. Westhoff, and J. Zupan, Integrating in the Higgs Portal to Fermion Dark Matter, *JHEP* **09**, 015, [arXiv:1506.04149 \[hep-ph\]](#).
- [20] L. Calibbi, A. Mariotti, and P. Tziveloglou, Singlet-Doublet Model: Dark matter searches and LHC constraints, *JHEP* **10**, 116, [arXiv:1505.03867 \[hep-ph\]](#).
- [21] C. Cheung and D. Sanford, Simplified Models of Mixed Dark Matter, *JCAP* **02**, 011, [arXiv:1311.5896 \[hep-ph\]](#).
- [22] S. Banerjee, S. Matsumoto, K. Mukaida, and Y.-L. S. Tsai, WIMP Dark Matter in a Well-Tempered Regime: A case study on Singlet-Doublets Fermionic WIMP, *JHEP* **11**, 070, [arXiv:1603.07387 \[hep-ph\]](#).
- [23] A. Dutta Banik, A. K. Saha, and A. Sil, Scalar assisted singlet doublet fermion dark matter model and electroweak vacuum stability, *Phys. Rev. D* **98**, 075013 (2018), [arXiv:1806.08080 \[hep-ph\]](#).
- [24] S. Horiuchi, O. Macias, D. Restrepo, A. Rivera, O. Zapata, and H. Silverwood, The Fermi-LAT gamma-ray excess at the Galactic Center in the singlet-doublet fermion dark matter model, *JCAP* **03**, 048, [arXiv:1602.04788 \[hep-ph\]](#).
- [25] D. Restrepo, A. Rivera, M. Sánchez-Peláez, O. Zapata, and W. Tangarife, Radiative Neutrino Masses in the Singlet-Doublet Fermion Dark Matter Model with Scalar Singlets, *Phys. Rev. D* **92**, 013005 (2015), [arXiv:1504.07892 \[hep-ph\]](#).
- [26] T. Abe, Effect of CP violation in the singlet-doublet dark matter model, *Phys. Lett. B* **771**, 125 (2017), [arXiv:1702.07236 \[hep-ph\]](#).
- [27] P. Konar, A. Mukherjee, A. K. Saha, and S. Show, Linking pseudo-Dirac dark matter to radiative neutrino masses in a singlet-doublet scenario, *Phys. Rev. D* **102**, 015024 (2020), [arXiv:2001.11325 \[hep-ph\]](#).
- [28] P. Konar, A. Mukherjee, A. K. Saha, and S. Show, A dark clue to seesaw and leptogenesis in a pseudo-Dirac singlet doublet scenario with (non)standard cosmology, *JHEP* **03**, 044, [arXiv:2007.15608 \[hep-ph\]](#).
- [29] L. Calibbi, L. Lopez-Honorez, S. Lowette, and A. Mariotti, Singlet-Doublet Dark Matter Freeze-in: LHC displaced signatures versus cosmology, *JHEP* **09**, 037, [arXiv:1805.04423 \[hep-ph\]](#).
- [30] P. Ghosh, P. Konar, A. K. Saha, and S. Show, Self-interacting freeze-in dark matter in a singlet doublet scenario, *JCAP* **10**, 017, [arXiv:2112.09057 \[hep-ph\]](#).
- [31] P. K. Das, P. Konar, S. Kundu, and S. Show, Jet substructure probe to unfold singlet-doublet dark matter in the presence of non-standard cosmology, *JHEP* **06**, 198, [arXiv:2301.02514 \[hep-ph\]](#).
- [32] S. Bhattacharya, S. Jahedi, and J. Wudka, Probing heavy charged fermions at e^+e^- collider using the optimal observable technique, *JHEP* **05**, 009, [arXiv:2106.02846 \[hep-ph\]](#).
- [33] R. Enberg, P. J. Fox, L. J. Hall, A. Y. Papaioannou, and M. Papucci, LHC and dark matter signals of improved naturalness, *JHEP* **11**, 014, [arXiv:0706.0918 \[hep-ph\]](#).
- [34] P. K. Paul, S. K. Sahoo, and N. Sahu, Anatomy of singlet-doublet dark matter relic: annihilation, co-annihilation, co-scattering, and freeze-in, *JCAP* **10**, 053, [arXiv:2412.02607 \[hep-ph\]](#).
- [35] R. T. D'Agnolo, D. Pappadopulo, and J. T. Ruderman, Fourth Exception in the Calculation of Relic Abundances, *Phys. Rev. Lett.* **119**, 061102 (2017), [arXiv:1705.08450 \[hep-ph\]](#).
- [36] M. Garny, J. Heisig, B. Lülfl, and S. Vogl, Coannihilation without chemical equilibrium, *Phys. Rev. D* **96**, 103521 (2017), [arXiv:1705.09292 \[hep-ph\]](#).
- [37] J. Abdallah *et al.* (DELPHI), Searches for supersymmetric particles in e^+e^- collisions up to 208-GeV and interpretation of the results within the MSSM, *Eur. Phys. J. C* **31**, 421 (2003), [arXiv:hep-ex/0311019](#).
- [38] G. Alguero, G. Belanger, S. Kraml, and A. Pukhov, Co-scattering in micrOMEGAs: A case study for the singlet-triplet dark matter model, *SciPost Phys.* **13**, 124 (2022), [arXiv:2207.10536 \[hep-ph\]](#).
- [39] J. Aalbers *et al.* (LZ), Dark Matter Search Results from 4.2 Tonne-Years of Exposure of the LUX-ZEPLIN (LZ) Experiment, *Phys. Rev. Lett.* **135**, 011802 (2025), [arXiv:2410.17036 \[hep-ex\]](#).
- [40] M. Cepeda *et al.*, Report from Working Group 2: Higgs Physics at the HL-LHC and HE-LHC, *CERN Yellow Rep. Monogr.* **7**, 221 (2019), [arXiv:1902.00134 \[hep-ph\]](#).
- [41] H. Lubatti *et al.* (MATHUSLA), Explore the lifetime frontier with MATHUSLA, *JINST* **15** (06), C06026, [arXiv:1901.04040 \[hep-ex\]](#).